

The infra-red luminosities of $\sim 332,000$ SDSS galaxies predicted from artificial neural networks and the Herschel Stripe 82 survey

Sara L. Ellison¹, Hossein Teimoorinia¹, David J. Rosario², J. Trevor Mendel²

¹ *Department of Physics & Astronomy, University of Victoria, Finnerty Road, Victoria, British Columbia, V8P 1A1, Canada.*

² *Max-Planck-Institut für Extraterrestrische Physik, Giessenbachstrasse, D-85748 Garching, Germany.*

16 August 2018

ABSTRACT

The total infra-red (IR) luminosity (L_{IR}) can be used as a robust measure of a galaxy’s star formation rate (SFR), even in the presence of an active galactic nucleus (AGN), or when optical emission lines are weak. Unfortunately, existing all sky far-IR surveys, such as the Infra-red Astronomical Satellite (IRAS) and AKARI, are relatively shallow and are biased towards the highest SFR galaxies and lowest redshifts. More sensitive surveys with the Herschel Space Observatory are limited to much smaller areas. In order to construct a large sample of L_{IR} measurements for galaxies in the nearby universe, we employ artificial neural networks (ANNs), using 1136 galaxies in the Herschel Stripe 82 sample as the training set. The networks are validated using two independent datasets (IRAS and AKARI) and demonstrated to predict the L_{IR} with a scatter $\sigma \sim 0.23$ dex, and with no systematic offset. Importantly, the ANN performs well for both star-forming galaxies and those with an AGN. A public catalog is presented with our L_{IR} predictions which can be used to determine SFRs for 331,926 galaxies in the Sloan Digital Sky Survey (SDSS), including $\sim 129,000$ SFRs for AGN-dominated galaxies for which SDSS SFRs have large uncertainties.

Key words: Methods: data analysis, methods: numerical, infra-red: galaxies, galaxies: active, galaxies: statistics, galaxies: fundamental parameters

1 INTRODUCTION

Galaxies evolve through the conversion of gas into stars. Galactic mass assembly over cosmic time is therefore largely characterized by the history of star formation. In turn, the star formation is modulated by both internal processes that may both trigger and quench star formation (e.g. Tan 2000; Ellison et al. 2011; Cheung et al. 2012; Saintonge et al. 2012; Wang et al. 2012; Mendel et al. 2013; Bluck et al. 2014; Forbes et al. 2014; Schawinski et al. 2014; Willett et al. 2015) as well as external gas replenishment from the inter-galactic medium and mergers (Keres et al. 2005; Sancisi et al. 2008; L’Huillier, Combes & Semelin 2012). Large samples of robust star formation rates are therefore critical for dissecting the processes that drive galaxy evolution.

Although galaxy scale star formation rates (SFRs) can be derived at many wavelengths, ranging from the X-ray to the radio (see Kennicutt 1998 and Kennicutt & Evans 2012 for reviews), the most common techniques (at low redshifts) use rest-frame ultraviolet (UV) and optical diagnostics. In the UV, the unobscured SFR is measured directly from the photons originating from the young stellar population. However, UV diagnostics must usually be combined with data at longer wavelengths in order to account for dust obscured star formation (e.g. Salim et al. 2007 and references therein). Optical emission lines suffer less from (but must still be

corrected for) the effects of dust obscuration, and represent one of the most widely used methods for measuring the SFR in the local universe. Such techniques either measure the strength of Balmer recombination lines (e.g. Kennicutt et al. 1994), which are a direct consequence of ionization by UV photons, or make use of empirical calibrations with forbidden lines such as [O II] (e.g. Kennicutt 1998). The main limitation of optical emission lines is contamination from ionizing processes that are not linked to young stars, such as interstellar shocks, active galactic nuclei (AGN) or planetary nebulae. The calibration between [O II] luminosity and SFR is also dependent on dust extinction and metallicity; if these parameters are not accounted for, additional scatter arises in the SFR calibration (Kewley, Geller & Jansen 2004). The measurement of the far infra-red (FIR) continuum, which probes emission from warm dust heated by star formation, provides a third complementary SFR measure. Beyond the mid-IR, contributions to the FIR from AGN should be negligible and can yield a robust measure of the total SFR (e.g. Netzer et al. 2007; Buat et al. 2010; Hatziminaoglou et al. 2010; Mullaney et al. 2011).

Despite its advantages, the application of FIR star formation rate diagnostics in the nearby universe has remained fairly limited, and the largest SFR samples currently available tend to rely on optical emission lines and the UV (Brinchmann et al. 2004; Salim et al. 2007; Gunawardhana et al. 2011). This limitation has been due

largely to the typically low sensitivity and low spatial resolution of FIR observing facilities. The former issue limits detections to only the highest SFR galaxies and the latter issue means that measurements may be contaminated by either other galaxies in the telescope beam or by Galactic cirrus (e.g. Takeuchi et al. 2010). The Herschel Space Observatory (Pilbratt et al. 2010; hereafter, simply Herschel) represents a dramatic improvement in both spatial resolution and in sensitivity. There are several extra-galactic surveys that have been conducted with Herschel, whose operations ceased in 2013. The largest is the Herschel Astrophysical Terahertz Large Area Survey (H-ATLAS, Eales et al. 2010), which covered over 550 sq. degrees and is predicted to yield many tens of thousands of detections of galaxies at $z < 0.3$. Indeed, in the Science Demonstration Phase (SDP), H-ATLAS covered 16 sq. degrees and detected ~ 3300 galaxies at $z < 0.2$ (Dariush et al. 2011). A review of FIR galaxy surveys, with an emphasis on Herschel’s impact, is given in Lutz (2014).

Whilst Herschel can provide robust SFRs for galaxies that are actively forming stars, it reaches its sensitivity limit for a SFR of $\sim 1 M_{\odot} \text{ yr}^{-1}$ at $z=0.08$ (Rosario et al. 2015). For example, the H-ATLAS survey finds that the $250 \mu\text{m}$ detection rate of low redshift galaxies with r -band magnitudes brighter than 18 is ~ 30 per cent (Dariush et al. 2011). Similar detection fractions are found from other Herschel galaxy surveys, such as the Herschel Multi-Tiered Extragalactic Survey (HerMES, Buat et al. 2010; Hatziminaoglou et al. 2010) and the Herschel Stripe 82 survey (Viero et al. 2014; Rosario et al. 2015). The importance of Herschel’s detection limit is poignantly demonstrated when a comparison is made with optical SFRs. In general, the SFRs of *actively star forming* galaxies derived from optical emission lines are in excellent agreement with those determined from Herschel FIR photometry (Dominguez Sanchez et al. 2012; Rosario et al. 2015). However, for galaxies with an AGN contribution, or weak emission lines there is an apparent offset between the optical SFRs in the Sloan Digital Sky Survey (SDSS) and those determined from the FIR (Fan et al. 2013; Matsuoka & Woo 2015). For these galaxies, the SDSS SFRs are derived from the 4000 \AA break, which correlates well with specific SFR in star-forming galaxies (see Brinchmann et al. 2004 for a complete description of this method), but uncertainties in the calibration lead to large uncertainties on the resulting SFR. Rosario et al. (2015) have shown that the apparent under-estimate of SDSS SFRs, relative to that derived from L_{IR} , for weak emission line galaxies and AGN is due to a combination of the limiting SFR detectable by Herschel, and the relatively large uncertainties on the optical SFRs for weak line and AGN galaxies. Therefore, despite its detection limit, Rosario et al. (2015) have demonstrated that Herschel is able to provide robust SFRs for classes of galaxies (such as those with low SFRs, or AGN contributions) that frequently have large uncertainties in their optical SFRs.

The promise of FIR star formation rates is currently limited by the size of the Herschel samples available. The final release of H-ATLAS data will be a dramatic step forward in this regard, but its sky coverage is still less than 10 per cent of the SDSS Data Release 7 (DR7) Legacy area. There are no imminent prospects for expanding deep FIR surveys; the next major IR facility will be the joint Japanese/European SPICA observatory, not due for launch for another decade. In this paper we investigate the possibility of using existing Herschel data as a training set for machine learning techniques that could be used to predict the L_{IR} for a large sample of nearby galaxies. We have previously used artificial neural networks (ANN) to predict emission line fluxes for galaxies in the

SDSS (Teimoorinia & Ellison 2014) and for ranking the parameters that drive galaxy quenching (Teimoorinia, Bluck & Ellison 2015).

The current paper is organized as follows. In Section 2 we describe the various IR observational samples and catalogs used in this work, for either training or verification of the ANN, the determination of L_{IR} , and consistency checks between these catalogs. In Section 3 we outline the basic ANN training procedure; the validation of the network is described in Section 4. The trained network is applied to the SDSS in Section 5, resulting in a catalog of $\sim 332,000$ galaxies with predicted IR luminosities, which is made publically available with this paper.

2 INFRA-RED OBSERVATIONAL SAMPLES AND CATALOGS

In this work we will make use of data from three separate spacecraft that collected data in the far-IR: the Infra-red Astronomical Satellite (IRAS, Neugebauer et al. 1984), AKARI (Murakami et al. 2007) and Herschel (Pilbratt et al. 2010). The first two of these missions were designed to perform all sky surveys that have public photometry available in their archives. However, as we will demonstrate later in this Section, AKARI and IRAS are limited to galaxies with relatively high SFRs. We therefore use data from the more sensitive Herschel mission as our training set. In contrast to AKARI and IRAS, Herschel operations combined targeted observations with survey science, including the H-ATLAS key program (Eales et al. 2010), of which only the 16 sq. degrees of the SDP are currently publically available. The public catalogs for the HerMES fields are the next largest dataset, covering a total of ~ 100 sq. deg. However, the different fields are observed to different depths (e.g. Fig 1 of Lutz 2014; see Oliver et al 2012 for a complete description of the multi-tiered approach), yielding a dataset with inhomogeneous detection thresholds, which is sub-optimal for training an ANN. Therefore, in order to train the network with the largest, homogeneous public dataset, which is critical for a robust learning pattern, we use the results from the Herschel Stripe 82 survey (Viero et al. 2014) which covers 79 sq. degrees.

Previous works have computed the total IR luminosity from these public catalogs. We review several of these works in the subsections below, but refer the interested reader to the original survey papers for full details on photometry and spectral fitting. However, since the ANN procedure involves training on one dataset, followed by validation with independent datasets¹, homogeneity between the catalogs is paramount. Systematic differences between L_{IR} derivations, e.g. due to different far-IR templates, will compromise the performance of the ANN predictions. Therefore, although we make use of the archival catalogs of IR photometry, we will derive all of our own IR luminosities.

We begin with a brief review of the characteristics of the IR data, the public catalogs and matches to the SDSS. We then describe the techniques applied homogeneously to the photometric catalogs to determine the total infra-red luminosities.

¹ When one large training set is available, it is common practice to train on a fraction of the data, and use the remainder for the independent validation. However, our training set is rather limited in number ($N=1136$), so that we risk compromising the training procedure if we reduce its input.

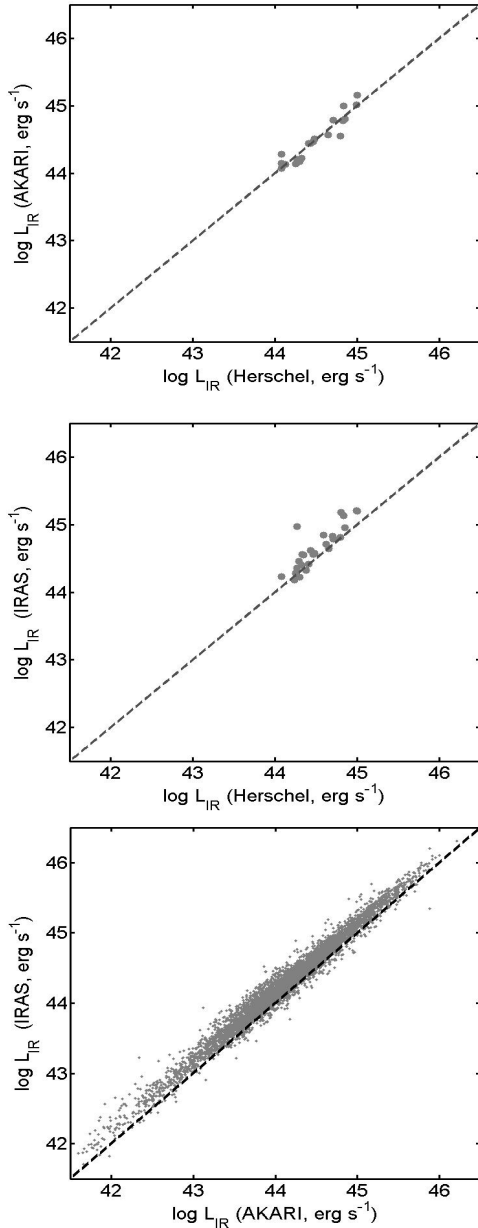


Figure 1. Comparison between derived L_{IR} for galaxies in common between the three catalogs considered in this work. Whereas AKARI and Herschel are in good agreement, the infra-red luminosities from IRAS are offset from the other two catalogs by ~ 0.15 dex

2.1 The IRAS All Sky Survey

IRAS (Neugebauer et al. 1984) surveyed the sky in four bands at 12, 25, 60 and 100 μm , with a spatial resolution ranging from approximately 0.5 arcmin to 2 arcmin at 12 and 100 μm respectively. Numerous works have matched galaxies in the SDSS to IRAS catalogs in order to study the IR properties of low redshift galaxies (e.g. Goto 2005; Wang et al. 2006; Obric et al. 2006; Wang & Rowan-Robinson 2009; Hwang et al. 2010, 2011; Wang et al. 2014). In this work, we use the catalog of Hwang et al. (2010), who matched the IRAS Faint Source Catalogue (FSC, Moshir et al. 1992), which contains 173,044 IR sources at $|b| > 10$ deg, with the SDSS DR7. As described by Hwang et al. (2010), the positional uncertainties in

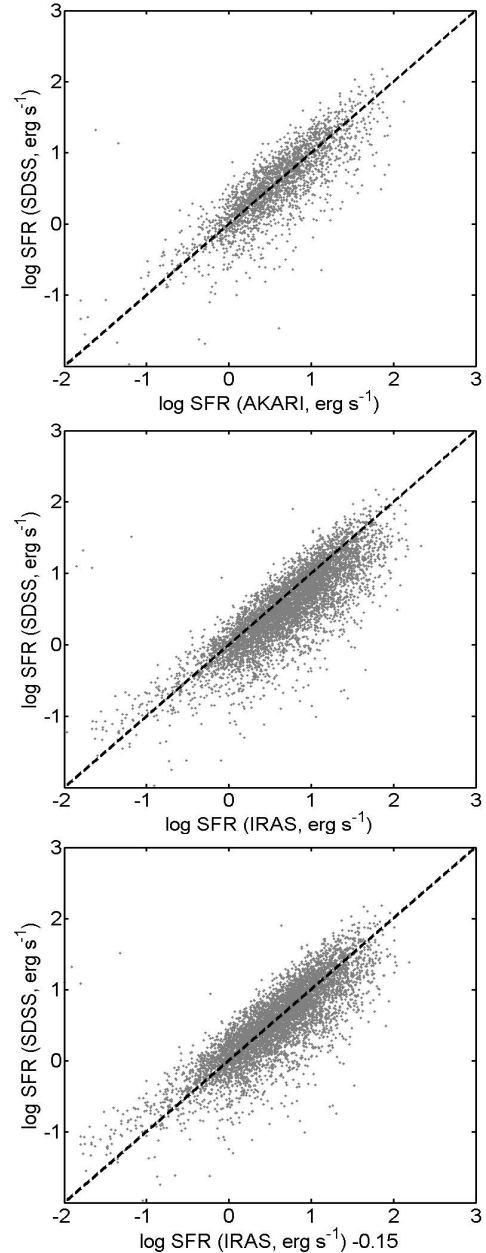


Figure 2. Comparison between the aperture corrected total SFRs (star-forming galaxies only) measured from the SDSS spectra and values inferred from L_{IR} (Eqn. 1) for AKARI (top panel) and IRAS (middle panel). The median offset of the IRAS fluxes derived from both the SFRs (this Figure) and L_{IR} (Figure 1) is 0.15 dex. The lower panel shows the SFRs derived from IRAS after this correction has been applied. A comparison between SFRs inferred for Herschel detected galaxies and the SDSS values is presented in Rosario et al. (2015), where an excellent agreement is found for star-forming galaxies.

the IRAS data are heterogeneous and depend on the scan direction. The positional uncertainty can be as small as 1 arcsec, ranging up to almost 1 arcmin. In order to match the IRAS detected sources with the SDSS, Hwang et al. (2010) used the individual source error ellipses and identified successful matches within 3σ of this positional uncertainty. This procedure yielded multiple matches for 10 per cent of IRAS detections, in which case the closest optical match was adopted. There are a total of 14,334 galaxies matched

between SDSS and IRAS with $60\ \mu\text{m}$ detections. Since the determination of L_{IR} (Section 2.4) includes mid-IR² photometry from the Wide Field Infra-red Survey Explorer (WISE, Wright et al. 2010), we limit our sample to $z < 0.3$ in order to avoid possible contamination of polyaromatic hydrocarbons (PAHs). After this limiting redshift is imposed, our final IRAS sample consists 14,255 galaxies for which L_{IR} is computed.

2.2 The AKARI/FIS All Sky Survey

The Far Infra-red Surveyor (FIS, Kawada et al. 2007) on board the AKARI satellite (Murakami et al. 2007) conducted an all sky survey at 65, 90, 140 and $160\ \mu\text{m}$ wavelengths. The nominal point spread functions of FIS are 37, 39, 58 and 61 arcseconds in these four wavebands, respectively (Kawada et al. 2007). The FIS Bright Source Catalog $90\ \mu\text{m}$ detected sources were matched to the SDSS DR7 by Hwang et al. (2011). A matching tolerance of 12 arcsec was adopted, which corresponds to AKARI's $2\ \sigma$ positional uncertainty. If multiple galaxies are matched, the closest one is adopted.

We once again make use of the positional matches of Hwang et al. (2011) but compute our own infra-red luminosities. Nonetheless, we have compared our derived L_{IR} values with those of Hwang et al. (2011), who used the Chary & Elbaz (2001) templates. In general there is very good agreement in the two sets of infra-red luminosities (the same is also true of a comparison between our IRAS fluxes and those of Hwang et al. 2010), where our L_{IR} determinations using the Dale & Helou (2002) templates are higher than those of Hwang et al. by ~ 0.03 dex on average. This is consistent with previous works (e.g. Goto et al. 2011) who have also concluded that robust L_{IR} determinations can be obtained independent of the choice of template. In total, there are 6965 galaxies with $90\ \mu\text{m}$ detections in the matched SDSS catalog; after the $z < 0.3$ cut, this results in a final AKARI sample of 6957 galaxies for which L_{IR} is derived.

2.3 The Herschel/SPIRE Stripe 82 Survey

The Herschel Stripe 82 survey (Viero et al. 2014) covers a total area of $79\ \text{deg}^2$ along an equatorial strip ($-2 < \delta < +2$) between 13 and 37 degrees in right ascension. The survey was conducted by the SPIRE instrument (Griffin et al. 2010) at 250, 350 and $500\ \mu\text{m}$, with a spatial resolution of 18.2, 25.2 and 36.3 arcseconds respectively. The catalog is $250\ \mu\text{m}$ selected, to a depth of $\sim 30\ \text{mJy}$ (3σ), which corresponds to a SFR of $1\ \text{M}_{\odot}/\text{year}$ at $z = 0.08$.

Rosario et al. (2015) matched the Herschel Stripe 82 catalog with galaxies present in the SDSS DR7 Main Galaxy Sample whose extinction corrected Petrosian r -band magnitudes are brighter than 17.77 and whose redshifts are in the range $0.04 < z < 0.15$. 3319 SDSS galaxies satisfying these criteria lie within the Herschel Stripe 82 footprint. The two catalogs were matched with a positional tolerance of 5 arcseconds, yielding 1349 matches; an IR detection rate of 40%. Rosario et al. (2015) also matched the SPIRE/SDSS detections with the public all sky survey conducted by WISE, with the requirement of a $S/N > 5$ in at least one of the 4 bands ($3.4, 4.6, 12$ and $22\ \mu\text{m}$) and positional tolerance of 2 arcsecs.

2.4 Derivation of L_{IR}

The mid- and far-IR photometry of galaxies from WISE and each of the FIR surveys described above, respectively, were fit with the galaxy SED templates of Dale and Helou (2002). This process is described in detail by Rosario et al. (2015), but we review the salient details here. IR luminosities were derived by integrating the best fit templates over rest-frame $8\text{--}1000\ \mu\text{m}$. The minimum requirement for a fit was a $S/N > 3$ detection in the selection band of the survey: IRAS $60\ \mu\text{m}$, AKARI $90\ \mu\text{m}$, or Herschel/SPIRE $250\ \mu\text{m}$. If a galaxy had $S/N > 2$ photometric measurements in other bands from the same survey, these were also used to constrain the fits. The exception is the IRAS $12\ \mu\text{m}$ band which we do not use, due to the possibility of contamination by AGN. In the case of Herschel galaxies, WISE $22\ \mu\text{m}$ photometry was used where available to constrain the short-wavelength part of the IR SED. We required that the additional bands covered rest-frame wavelengths redwards of $20\ \mu\text{m}$ to avoid any strong effects from PAHs or AGN-heated dust.

Since the selection band is also the most sensitive in each of these surveys, a substantial fraction of galaxies were only detected in this single band. In these cases, we estimated L_{IR} by scaling the photometry to a fixed IR template, corresponding to an M82-like SED (see Rosario et al. 2015 for more details about rationale for this choice of template.)

2.5 Calibration consistency

We now have in hand three separate IR catalogs that have been matched to the SDSS and for which we have computed the L_{IR} . Before discussing how the ANN training and validation sets are selected, we must first confirm that the different IR datasets are consistently calibrated. Despite the adoption of a uniform spectral template fitting procedure, the measurement of the input photometry is heterogeneous, the compilation of catalogs is performed at different wavelengths and the range in spatial resolution between instruments may also result in varying degrees of contamination or SDSS matching errors.

We perform the consistency checks between IR catalogs in two ways. First, we identify the galaxies that are in common between the three surveys, resulting in 20 galaxies matched between Herschel Stripe 82 and AKARI, 26 galaxies between Herschel and IRAS and 5860 between IRAS and AKARI. In Figure 1 we compare the L_{IR} of these common galaxies. For the galaxies common between the AKARI and Herschel Stripe 82 catalogs, the L_{IR} are in excellent agreement, with no systematic offset (Fig. 1, top panel). However, the common galaxies in Herschel and IRAS are slightly offset from the 1:1 relation by a mean value of 0.14 dex (Fig. 1, middle panel), although the number of galaxies is small. The offset is more obvious between AKARI and IRAS, thanks to the larger dataset (Fig. 1, bottom panel), in which the mean offset for ~ 6000 galaxies is 0.15 dex.

Due to the relatively small overlap between the Herschel Stripe 82 SDSS sample and either AKARI or IRAS, we perform a second test of the consistency between catalogs. In Rosario et al. (2015) we showed that, for star forming galaxies, the SFRs inferred from the Herschel L_{IR} are in excellent agreement with the values derived from the aperture corrected SDSS spectra. We therefore similarly use the SDSS total SFRs to verify the L_{IR} values of AKARI and IRAS. We adopt the conversion between L_{IR} and SFR from Kennicutt (1998), with an adjustment for a Chabrier initial mass function (IMF):

² Unless otherwise stated, all mid-IR photometry in this paper comes from WISE.

$$\log L_{IR} = \log SFR + 43.591 \quad (1)$$

SDSS SFRs are taken from the public MPA/JHU catalogs³. The techniques used to determine total SFRs for SDSS galaxies are described in detail by Brinchmann et al. (2004) and Salim et al. (2007), but we review the salient details here. The fibre spectra are fit with models from Charlot & Longhetti (2001), which combine stellar continuum templates with emission lines simulated by the Cloudy software (Ferland et al. 1998). The models are run over large grids of input parameters, including dust attenuation, metallicity and star formation rate. Likelihood distributions are constructed using a Bayesian approach, from which the median is taken as the ‘best’ value. Errors on SFRs are derived from the full probability distribution functions. Although the models fit the entire SDSS spectrum, the derived SFRs are dominated by the strength of the Balmer emission lines. However, Brinchmann et al. (2004) note that contributions to emission lines from processes not related to star formation will lead to erroneous SFRs. Such processes include shocks, planetary nebulae and AGN. Brinchmann et al. (2004) therefore identify galaxies with either a minor (‘composite’) or dominant AGN contribution using emission line fluxes and the diagnostic diagrams of Kewley et al. (2001) and Kauffmann et al. (2003). For both the composite and AGN galaxies, the SFR is determined from the correlation between D_{4000} and specific SFR (SSFR), as measured in the star-forming population. Errors on SFRs derived from D_{4000} are computed by convolving the likelihood distribution of a given galaxy’s D_{4000} with that of the relation between SSFR and D_{4000} in star forming galaxies. For all galaxy classes, the ‘fibre’ SFRs are converted to total SFRs by assessing the photometry outside of the aperture.

In Figure 2 we plot the SFRs derived (using Eqn. 1) from the observed (AKARI or IRAS) infra-red luminosities compared with the aperture corrected values derived from the SDSS spectra for star forming galaxies (Kauffmann et al. 2003). In the top panel, we see that the bulk of the SDSS star-forming galaxies in the AKARI catalog follow the 1:1 relation. There is a minority of galaxies that seem to have large AKARI SFRs compared to the SDSS values; these may be cases where the relatively large AKARI beam is picking up additional IR flux from a neighbouring object. We check this hypothesis by visually inspecting the SDSS images for all galaxies with $\log \text{SFR}(\text{AKARI}) - \log \text{SFR}(\text{SDSS}) > 0.6$ dex and find that the majority are indeed in close pairs, or have multiple companions. Additionally, we rule out higher extinctions in these galaxies as the explanation for the SFR offsets, since these galaxies have unremarkable values of $E(B-V)$, as derived from the Balmer decrement. In the middle panel of Figure 2, the same minority population with large offsets is seen for the IRAS detections. However, even the bulk of the IRAS SFRs seem to be slightly over-estimated relative to the SDSS values, consistent with the results of Figure 1. Once again, the median offset required to bring the IRAS infra-red luminosities into agreement with the SDSS SFRs is 0.15 dex. In the lower panel of Fig. 2 we show that, after a downwards correction of 0.15 dex applied uniformly to the IRAS infra-red luminosities, the IRAS L_{IR} values are now, on average, in good agreement with the SFRs of star-forming galaxies in the SDSS.

The presence of an offset between AKARI and IRAS L_{IR} has been previously reported by Takeuchi et al. (2010), who constructed full SEDs extending from the UV to the far-IR using GALEX, SDSS, 2MASS, IRAS and AKARI. Takeuchi et al. (2010)

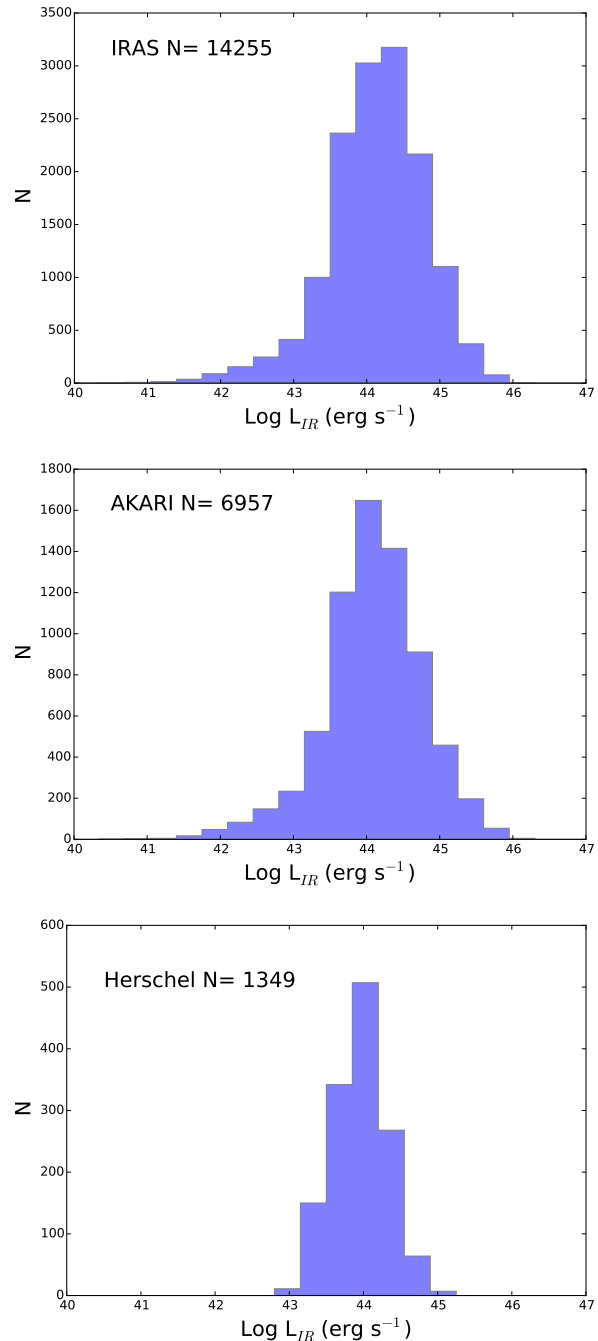


Figure 3. The distribution of the measured L_{IR} values for the SDSS matched galaxies in the IRAS (top panel), AKARI (middle panel) and Herschel Stripe 82 (lower panel) datasets.

demonstrate that the IRAS 60 and 100 μm fluxes consistently over-estimate the AKARI 65 and 90 μm photometry, suggesting that this is due to increased contamination, e.g. by Galactic cirrus or nearby sources, in the large IRAS beam (see also Takeuchi & Ishii 2004 and Jeong et al. 2007).

In summary, we find that there is good agreement between the L_{IR} determined from Herschel, AKARI and that inferred from the SDSS SFRs, but that IRAS IR luminosities are systematically over-estimated. When IRAS L_{IR} s are used in the remainder of this paper, they are always corrected downwards by 0.15 dex.

³ <http://home.strw.leidenuniv.nl/~jarle/SDSS/>

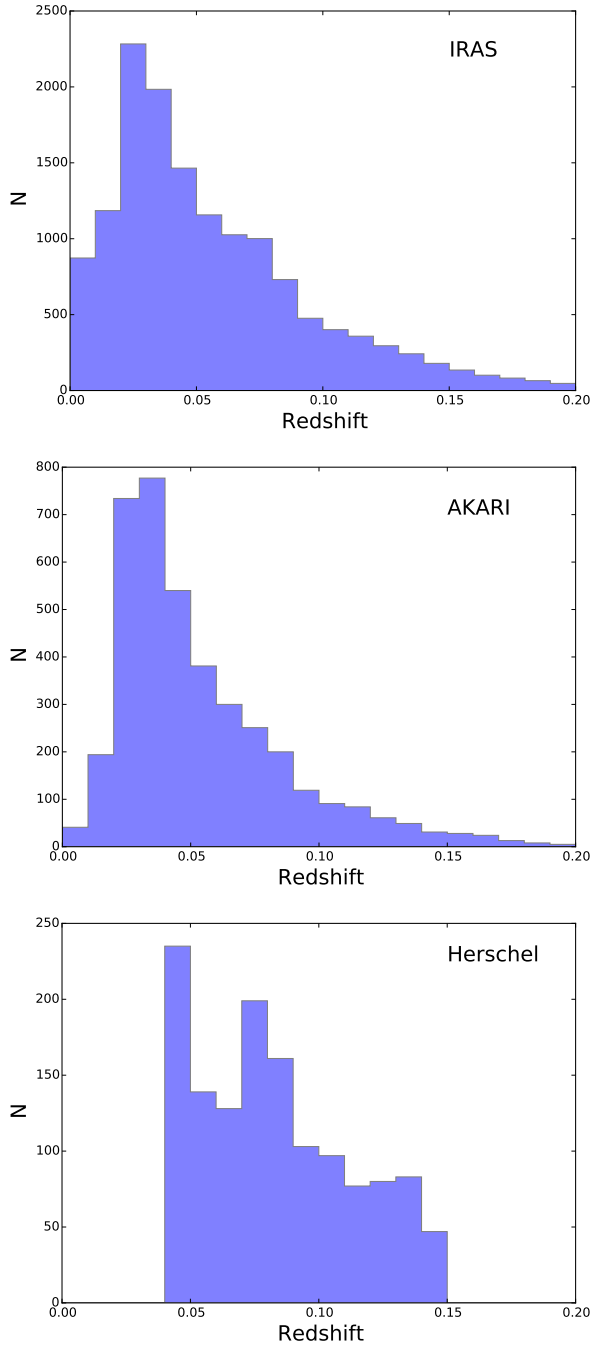


Figure 4. The distribution of redshifts for the SDSS matched galaxies in the IRAS (top panel), AKARI (middle panel) and Herschel Stripe 82 (lower panel) datasets.

2.6 Survey comparisons

Having established consistency between the L_{IR} calibrations of the three surveys used in this work, it is now useful to compare their relative properties, for example in terms of depth and redshift range. In Figures 3 and 4 we compare the distributions of L_{IR} and redshifts between the 3 surveys discussed above. The range of L_{IR} between the three surveys is quite similar, with most galaxies in the interval $43 < \log L_{IR} < 45$ erg/s, with the distribution peaking at $\log L_{IR} \sim 44$ erg/s. The range for Herschel is somewhat narrower

than AKARI or IRAS; the highest luminosity galaxies are rare and therefore not expected to be frequent in small area surveys. Despite its enhanced sensitivity, Herschel also has fewer of the lowest luminosity sources. These can only be detected by AKARI and IRAS at very low redshifts, the effective volume for which is again small for the Herschel Stripe 82 sample (particularly given the imposition of a low z cut-off for the Herschel sample).

Figure 4 shows that the Herschel detected sources are biased towards considerably higher redshifts, on average, than AKARI and IRAS. Indeed, the redshift distribution of Herschel (whose median value is 0.08) is closer to that of the complete SDSS Main Galaxy spectroscopic sample (whose median redshift is 0.10), whereas AKARI and IRAS are strongly biased towards relatively nearby galaxies (median redshifts of 0.042 and 0.055 respectively). The combination of similar L_{IR} distributions, but different redshift ranges, indicates that the AKARI and IRAS samples are likely biased towards galaxies with relatively high SFRs.

In Figure 5 we show the total SFRs compared to the stellar masses, the so-called star-forming main sequence. Star forming galaxies in the SDSS are shown in all three panels as blue filled contours for reference, where their SFRs are the aperture corrected values derived from the SDSS spectra. Data points indicate the SFRs derived from IR luminosities for each of the three IR surveys, computed using Eqn. 1. Figure 5 confirms that both AKARI and IRAS detected galaxies are biased towards galaxies that have relatively high SFRs for their stellar mass, whereas galaxies in the Herschel Stripe 82 sample are more typical of the star-forming population as a whole. There is also a significant population of Herschel detected galaxies at relatively high masses that are below the main sequence. Many of these are AGN dominated galaxies (using the diagnostic of Kauffmann et al. 2003); the results of Fig. 5 are therefore consistent with previous results that low redshift optically selected AGN in the SDSS can lie either on the main sequence or exhibit lower SFRs for their mass than star-forming galaxies (e.g. Salim et al. 2007; Gurkan et al. 2015)

In order to quantify the deviations from the main sequence we define a SFR offset, that accounts not just for the mass dependence of the main sequence but also redshift and local density. For every IR detected galaxy, we assemble a set of matched comparison galaxies from the SDSS star forming sample (no IR detection required). The comparison galaxies are required to have the same stellar mass, redshift and local density as the IR detected galaxy, within some tolerance. Local density is defined as

$$\Sigma_n = \frac{n}{\pi d_n^2}, \quad (2)$$

where d_n is the projected distance in Mpc to the n^{th} nearest neighbour within ± 1000 km s $^{-1}$. Normalized densities, δ_n , are computed relative to the median Σ_n within a redshift slice ± 0.01 . In this study we adopt $n = 5$ (although we note that the results of our work do not rely on the choice of n).

The baseline tolerance used for matching is 0.1 dex in stellar mass, 0.005 in redshift and 0.1 dex in δ_5 . We require at least 5 comparison galaxies for each IR detected galaxy; if this is not achieved the mass, redshift and local density tolerances are grown in further increments of 0.1 dex, 0.005 and 0.1 dex respectively, until the minimum size criterion of 5 is met. However, there are typically several tens of comparisons for each IR detected galaxy without the need to extend the tolerances. The median log SFR of the matched comparison sample is subtracted from the log SFR of the IR detected galaxy in order to determine the SFR offset, Δ SFR, from the main sequence.

In Figure 6 we quantify the visual impression of elevated SFRs in the IRAS and AKARI samples from Fig. 5 by plotting the distribution of Δ SFR (the logarithmic SFR offset) for the three IR samples. The Herschel Stripe 82 sample (red histogram) has a median offset of approximately zero, demonstrating that these galaxies are generally drawn from the normal star-forming main sequence. In contrast, both the AKARI and IRAS samples (blue and green histograms respectively) are strongly skewed to positive Δ SFR. The galaxies detected in these two surveys are typically forming stars at rates 2–3 times higher than their comparison galaxies (i.e. at fixed stellar mass, redshift and environment). AKARI and IRAS are therefore not suitable training sets for the ANN, since training with biased data will yield a network that similarly predicts SFRs that are relatively high. Nonetheless, AKARI and IRAS can still be used as validation sets. Indeed, it is a good test of the network’s reliability if it is able to accurately predict the characteristics of a sample whose properties contrast with its training set.

In summary of this section: we have homogeneously determined the IR luminosities of 14,255 galaxies in IRAS all sky survey, 6957 galaxies in the AKARI all sky survey and 1349 galaxies in the Herschel Stripe 82 survey that have matches in the SDSS spectroscopic survey. The IRAS photometry yields L_{IR} values that are offset by 0.15 dex from what we expect based on their SDSS SFRs; a similar offset is seen in the comparison of L_{IR} for galaxies in common between IRAS and either AKARI or Herschel. We also show that AKARI and IRAS are biased towards relatively high SFR galaxies, whereas the Herschel Stripe 82 sample is a good representation of star-forming galaxies at its median redshift of $z \sim 0.08$. For these reasons, the Herschel sample is our preferred training sample. Although it is the smallest of the three catalogs, its population is unbiased and its photometry is accurate (see also Rosario et al. 2015).

3 THE ARTIFICIAL NEURAL NETWORK AND DETERMINATION OF INFRA-RED LUMINOSITIES

Although many varieties of ANN exist, all of which can be configured, trained and optimized to solve various data challenges, the basic functionality of these techniques is similar. Based on a collection of input (training) data, the network derives a set of optimal weights and biases that best describes the relation to the target data. In this way, an ANN can be used to ‘predict’ target values for an independent dataset from its input variables. There is a vast literature available on the topic of ANN (e.g. Chen et al 1991; Battiti 1992; De Jesus & Hagan 2007), including its application to astronomical data problems (Andreon et al. 2000; Ball et al. 2004; Teimoorinia 2012; Gonzalez-Martin et al. 2014; Teimoorinia & Ellison 2014). Here we provide a high level overview of the statistical techniques adopted in the current work, referring the reader to technical papers (e.g. Bishop 2007) for more details.

3.1 Training parameters

The ultimate objective of the current work is to train a network that will predict the L_{IR} for a large fraction of the galaxies in the SDSS, as justified in the Introduction. The starting point of this work is therefore the identification of a sizable, high quality and homogeneous dataset for which we have a wide variety of galaxy parameters from SDSS available for training, and matched IR luminosities to act as the target data. The procedure will then be to train the network to recognize the linkages between SDSS parameters and L_{IR} ,

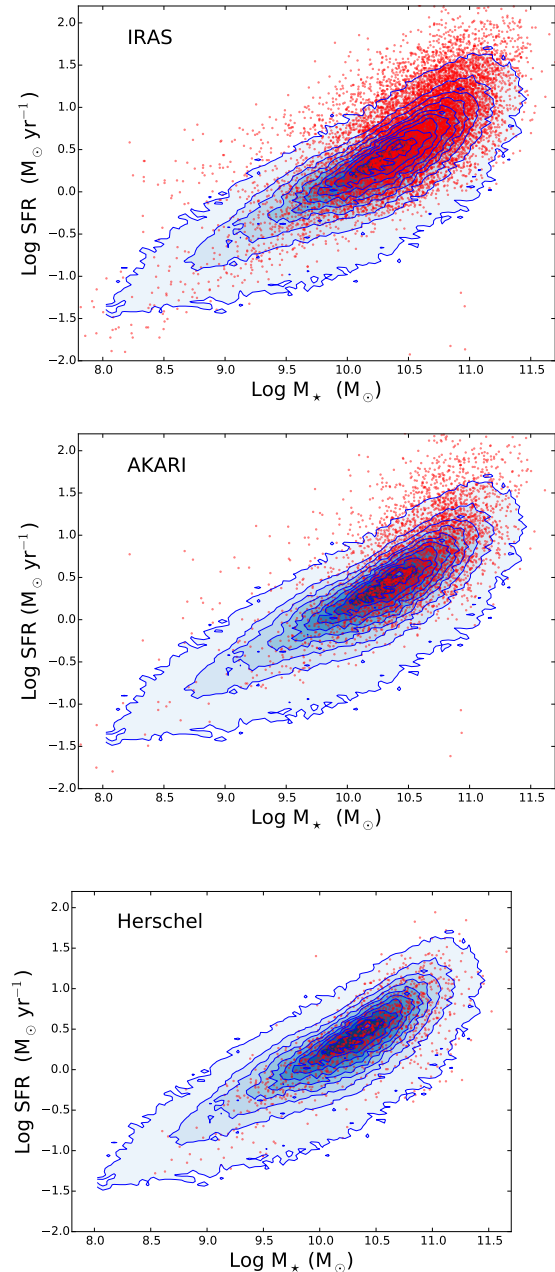


Figure 5. The star-forming main sequence for SDSS galaxies (filled contours in each panel) and SDSS matched galaxies in the IRAS (top panel), AKARI (middle panel) and Herschel Stripe 82 (lower panel) datasets. The SFRs for the SDSS star-forming galaxies are derived from aperture corrected spectroscopic values for galaxies classified as star-forming using the Kauffmann et al. (2003) diagnostic. The SFRs for IR-detected galaxies are derived from the infra-red luminosities using Eqn. 1 and shown as small points in each panel.

and then apply the trained network to predict the L_{IR} for the rest of the SDSS.

Fortunately, there are numerous public catalogs of SDSS galaxy properties, both measured and derived, from both spectroscopic and photometric products (e.g. Kauffmann et al. 2003; Brinchmann et al. 2004; Simard et al. 2011; Mendel et al. 2014). From this extensive vault of data, we experimented with various combinations of training parameters. Since the infra-red luminos-

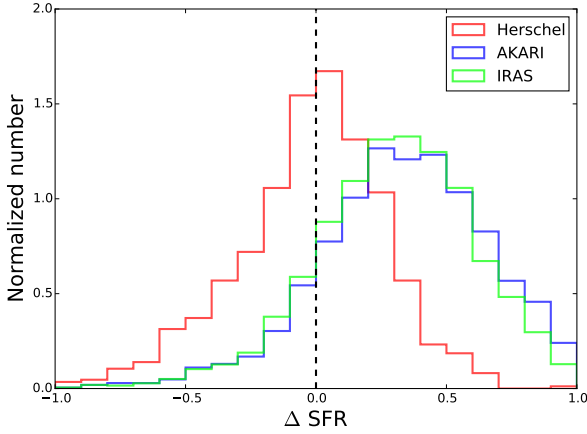


Figure 6. The offset of IR detected galaxies from the star-forming main sequence defined by star-forming galaxies in the SDSS with the same stellar mass, redshift and local density. The Herschel Stripe 82 sample (red histogram) has a median offset ($\Delta \text{SFR} = \log \text{SFR}(\text{IR detected galaxy}) - \log \text{SFR}(\text{comparison median})$) of approximately zero, implying that the sample is a good representation of normal star-forming galaxies. However, the AKARI (blue) and IRAS (green) samples are skewed towards positive SFR offsets; on average, the galaxies detected in these two surveys have SFRs higher by a factor of 2–3 compared to normal star forming galaxies.

ity is largely determined by the galaxy’s SFR, our first attempts at network training focussed on the combination of stellar mass, the fluxes of various emission lines and the strength of the 4000 Å break. Emission line fluxes are taken from the public MPA/JHU catalogs, that have been corrected for underlying stellar absorption and Galactic extinction. We apply further corrections to the line fluxes for internal extinction as described in Scudder et al. (2012) by adopting a Small Magellanic Cloud (SMC) extinction curve (Pei 1992), before converting the fluxes to luminosities.

In recognition of the limiting fibre aperture, we included both total and fibre stellar masses in the training set, as well as the explicit covering fraction of the r -band light. It was found that the network’s performance could be further improved with the provision of colours and absolute magnitudes. We also experimented with various morphological information (based on the bulge-disc decompositions of Simard et al. 2011), but no significant improvement was obtained. Our final set of training parameters is presented in Table 1. There are 8602, 3153 and 1136 galaxies in the IRAS, AKARI and Herschel Stripe 82 sample, respectively, for which all 23 of these parameters are available, where the majority of the IRAS and AKARI galaxies have been excluded due to their bright optical magnitudes which preclude them from many of the SDSS spectroscopic samples (e.g. Simard et al. 2011; Mendel et al. 2014).

3.2 Training algorithms and error estimation

After configuring the network for the input data, the main task of the ANN is to determine the appropriate weights and biases that best connect them to the target data. This is an iterative process, and can be achieved with different algorithms that are variously suited to different data situations. In the current work we derive the weights and biases according to the Levenberg-Marquardt optimization method (Marquardt 1963). This common technique minimizes a combination of squared errors and weights (Eq. 3), and then determines the correct combination. An adaptation to the basic Levenberg-Marquardt optimization, that may help to produce a

Table 1. The parameters used in work as input data for training and validation sets.

$M_{\star, \text{fibre}}$: Fibre stellar mass
M_{\star} : Total stellar mass
Corrected luminosity of [OII] λ 3727 Å emission line
Corrected luminosity of [OII] λ 3729 Å emission line
Corrected luminosity of [OIII] λ 4959 Å emission line
Corrected luminosity of [OIII] λ 5007 Å emission line
Corrected luminosity of H α λ 6563 Å emission line
Corrected luminosity of H β λ 4861 Å emission line
Corrected luminosity of [NII] λ 6582 Å emission line
Corrected luminosity of [SII] λ 6717 Å emission line
Corrected luminosity of [SII] λ 6731 Å emission line
z : Redshift
D_{4000} : 4000 Å break
r -band covering fraction
M_u : absolute u -band magnitude
M_g : absolute g -band magnitude
M_r : absolute r -band magnitude
M_i : absolute i -band magnitude
M_z : absolute z -band magnitude
u - g observed colour
g - r observed colour
r - i observed colour
i - z observed colour

network that generalizes well, is the addition of a Bayesian regularization term. The addition of the Bayesian regularizer is particularly useful if the training set is not very large (e.g., Neal, 1996). Specifically, we define the error function of the weights (\mathbf{W}) as

$$\text{Err}(\mathbf{W}) = \sum_{i=1}^N [Y(\mathbf{X}_i, \mathbf{W}) - T_i]^2 + \lambda \mathbf{W}^T \mathbf{W} \quad (3)$$

in which Y and T are the output of the network and the target values, and \mathbf{X} are the input data (in this case, the variables listed in Table 1) for N galaxies. The Bayesian regularization approach is important in the control of the so-called ‘over-fitting problem’ (Bishop 2007), which can occur when we use a powerful network (i.e., a network with large number of neurons) or the number of iterations in the training step (for updating the weights) is large. Over-fitting is also a pitfall associated with having a small training set. The Bayesian regularization mitigates the potential for over-fitting by adding a term to the squared error function (the first term in equation 3); this is sometimes referred to in ANN models as weight decay. In Eq. 3, the coefficient λ governs the relative importance of the regularization term compared with the error function of Eq. 3.

In many situations, the Levenberg-Marquardt algorithm can be successfully used to minimize only the first term of Eq. 3, removing the need for the Bayesian regularization. To demonstrate the differences between the two methods (with and without Bayesian regularization), we use a powerful network ($N_{\text{neuron}}=50$) and also use a large number of iterations to update the weights with the Herschel data used as the training set. The result can be seen in Figure 7. In the Bayesian regularization approach, no significant improvement in the network performance can be seen after ~ 20 iterations (the blue dashed line). If we minimize only the first term of Eq. 3 the result will show a better performance for higher iterations (red dashed line) but it has tendency to be over-fitted, so it is not suitable for generalization. For a more secure result, it is desirable to decrease the number of neurons, if the reduction does

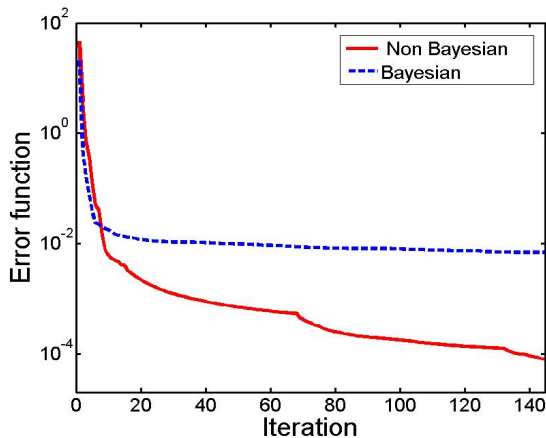


Figure 7. The performance of Levenberg-Marquardt optimization method without (solid line, the first term in equation 3) and with a Bayesian regulator term (dashed line, addition of the second term in equation 3) for a network using 50 neurons. Without the Bayesian regulator, there is a continued improvement as the number of iterations increases, indicative of an over-fitting problem. The addition of the Bayesian regularization shows convergence.

not decrease the performance of the network. In this work, we have found that decreasing the number of neurons to ~ 15 still yields an almost identical output as the more powerful 50 neuron network shown by the blue line in Figure 7, and with no absolute improvement after ~ 50 iterations.

The network is now fully trained and ready to be applied to a target dataset. The ultimate target dataset (we will investigate some validation sets in the following section) is the complete SDSS, for which all 23 parameters listed in Table 1 are available (331,926 galaxies). However, although we have shown that the Herschel Stripe 82 sample contains typical star forming galaxies, the training set may not be representative of *all* galaxies. Although the network can extrapolate well behaved correlations, it may not yield accurate predictions in cases where the target data exhibit different properties to the training set. We therefore develop a technique to identify galaxies with less secure L_{IR} predictions.

First, to avoid any bias and to obtain a statistical result, we repeat the training procedure 25 times and select the best 20 trained networks. This step is necessary because sometimes the initialization of the parameters can yield a solution with very high scatter, indicating that the network was not well trained, e.g. it has converged on a local, rather than global minimum in parameter space. The output of the best 20 trained networks show small differences due to the different initializations. The average value of the predicted L_{IR} for a given galaxy is computed as $(\mathbf{W}_k)^T \mathbf{X}$ for $k=1$ to 20, where \mathbf{W}_k are the weights obtained from the 20 best trained networks. Since \mathbf{W}_k have been determined for the Herschel input parameter space, for those galaxies in the SDSS sample that have very different input data, \mathbf{X} , the scatter will be very large. On the other hand, for the galaxies that have input parameter space similar to Herschel's, the variations should be small, because the weights and biases are tailored for this input data. We adopt the mean L_{IR} value of the 20 best trained networks, and assign the associated 'error' (σ_{ANN}) as the scatter amongst the network outputs. This error does not encapsulate the uncertainties in the calibration itself, nor those associated with the input data. Rather, it provides a con-

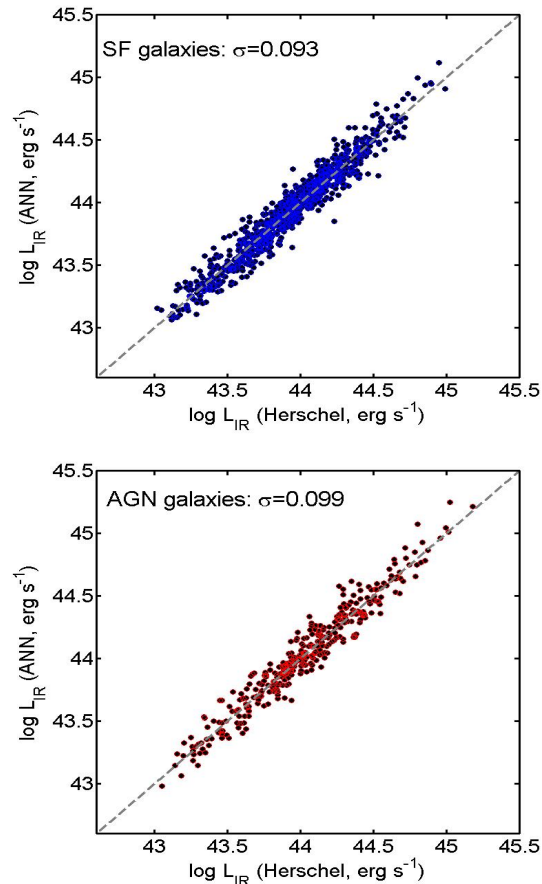


Figure 8. Self validation of the ANN with Herschel Stripe 82 data. The ANN-predicted L_{IR} is compared with observed infra-red luminosities for the training sample. The top panel shows the results for galaxies classified as star-forming (Kauffmann et al. 2003) and the lower panel for AGN. The network is well trained for both galaxy classifications.

fidence indicator for the network predictions, which we will later use to identify robust samples.

4 NETWORK VALIDATION

4.1 Self validation

The first validation check involves an internal (self) validation with the training dataset. If the network is well trained, the performance of the self-validation should be good. In Figure 8 we show the predicted L_{IR} from the ANN compared to the Stripe 82 luminosities. We assess the performance of the ANN separately for star-forming galaxies and those with an AGN. Throughout this paper we distinguish AGN using the Kauffmann et al. (2003) classification, with a $S/N > 1$ requirement in all 4 necessary lines. In the top panel of Figure 8, we show the results for the star-forming galaxies; the performance is excellent, with a scatter between the observed and predicted L_{IR} of only 0.093 dex. Such a small scatter is expected for three reasons. First, in the self validation step we are testing on the data used to train the network, so we know that the optimum weights and biases for this dataset are being applied. Second, of the 23 input parameters used (Table 1), several (such as the emission line fluxes) are known to correlate very well with SFR, and should

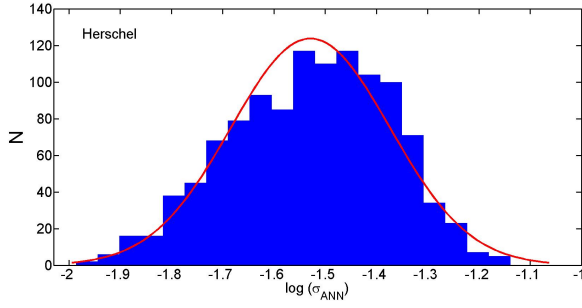


Figure 10. The distribution of σ_{ANN} in the Herschel training set. A Gaussian fit to the distribution is shown in red.

hence be excellent indicators of L_{IR} . Finally, the star-forming sample represents the bulk of the training set (892/1136 galaxies). In the lower panel of Figure 8 we show the performance of the AGN dominated galaxies. Again, the performance is excellent, with a scatter of 0.099 dex, indicating that the network is equally well trained and applicable to galaxies with an active nucleus. This is a non-trivial result: the emission lines in AGN galaxies have contributions from more than one photo-ionizing source. Therefore, in contrast to the star-forming galaxies, there is no *a priori* mapping between emission line fluxes, SFRs and L_{IR} . Nonetheless, the ANN is able to combine the inputs of all the parameters, with appropriate weights and biases, to determine a solution for L_{IR} that is applicable even when the AGN ‘contamination’ is present.

4.2 Validation with independent datasets

Whilst the results of the self-validation are re-assuring, the next critical step is to validate the ANN on independent datasets; AKARI and IRAS are used for this purpose. Before investigating in detail the performance of the independent validation, it is useful to quantify the effect of cuts in σ_{ANN} on the two datasets. We define ΔL_{IR} as the difference between the ANN predicted L_{IR} and the measured value. In Fig. 9 we show the scatter ($\sigma_{L_{\text{IR}}}$) in ΔL_{IR} for the AKARI and IRAS datasets, as a function of σ_{ANN} threshold. The choice of where to put the error threshold is a trade-off between the size of the sample for which L_{IR} is predicted, and the likely scatter in those predictions, and different thresholds in σ_{ANN} will be appropriate for different applications. In Fig. 10 the distribution of σ_{ANN} for the Herschel training set is plotted, with a Gaussian fit overlaid. The tail of the Gaussian distribution extends to $\sigma_{\text{ANN}} \sim 0.1$ which we adopt as a working threshold for the remainder of this paper.

4.2.1 AKARI validation

In the top panel of Figure 11 we compare the ANN-predicted and AKARI L_{IR} for the 2649 galaxies whose ANN error is $\sigma_{\text{ANN}} < 0.1$ dex, with points colour-coded by the density of galaxies in each cell. Recall that σ_{ANN} is determined from the distribution of L_{IR} over 20 different initializations of the training, and is a reflection of the similarity of the input variables of a given test galaxy and the training set. The scatter in the comparison between measured AKARI IR luminosities and those predicted by the ANN after the $\sigma_{\text{ANN}} < 0.1$ dex threshold has been imposed is 0.22 dex, with a symmetric scatter. Although this scatter is higher than for the self validation (which is to be expected), there is no systematic offset between the prediction and observed L_{IR} . As noted in Section 2.2, at

least part of the increase in scatter in the comparison with AKARI is likely due to larger uncertainties in AKARI’s photometry. Indeed, we experiment with using AKARI as the initial training set and find that it has a much higher internal scatter than the Herschel data.

In the middle and lower panels of Figure 11 we impose the same error cut of 0.1 dex, but now separate the galaxies that are classified as star-forming or AGN. The scatter in the two subsamples is very comparable, 0.20 dex and 0.24 dex for the star-forming and AGN classes, respectively, demonstrating that the single network can equally well be used to derive infra-red luminosities independently of the emission line classification.

4.2.2 IRAS validation

Despite the presence of an offset between the IRAS photometry and that of Herschel and AKARI, the IRAS dataset can still play a useful role in the validation of our trained network, thanks to its very large size. Recall that a 0.15 dex correction is applied to the IRAS IR luminosities in order to account for this offset. As was shown in the lower panel of Fig. 2, once the offset is applied, there is a good average agreement between the SDSS SFRs and IRAS L_{IR} .

In Figure 12 we compare the ANN predictions with the corrected IRAS L_{IR} for 7299 (out of a total of 8602 for which L_{IR} have been predicted) galaxies that have $\sigma_{\text{ANN}} < 0.1$ dex. The top panel shows the scatter for all galaxies, and the middle and lower panels distinguish star-forming and AGN galaxies, analogous to the AKARI validations shown in Figure 11.

Once the IRAS L_{IR} have been corrected for the known offset from AKARI, Herschel and SDSS, the top panel of Figure 12 demonstrates that there is good agreement between the predicted and observed infra-red luminosities, with a scatter of 0.24 dex. The scatter amongst the star-forming and AGN galaxies is 0.23 and 0.25 dex, respectively. The performance of the validation is therefore very similar for both the AKARI and IRAS datasets.

As part of the validation process, we have also checked that ΔL_{IR} (the difference between the predicted and measured luminosities) shows no residuals with any of the input parameters, and confirm that there is no systematic trend or offset with any of the parameters listed in Table 1. As a final additional check, we confirm that the scatter in ΔL_{IR} is not driven by the relative position of a galaxy in the star forming main sequence (stellar mass versus star formation rate). That is, we verify that we can equally well predict L_{IR} for galaxies that have relatively high or low SFRs for their stellar mass, as well as for those that are more typical. In Fig. 13 for star-forming galaxies only, we plot ΔL_{IR} as a function of ΔSFR (the offset of a given galaxy from the main sequence, as described in Section 2.6) for the Herschel, AKARI and IRAS samples. It can be seen that there is, in general, no correlation between ΔL_{IR} and ΔSFR , indicating that the scatter in the former is not driven our inability to predict L_{IR} for main sequence outliers. For the (rare) galaxies with very high SFR enhancements ($\Delta \text{SFR} > 0.8$, or a factor of 6 above the main sequence) in AKARI and IRAS there is a tendency of the ANN to modestly over-predict the L_{IR} ; this is likely due to the lack of such galaxies in the Herschel training set. Remaining sources of scatter could be physical parameters not included in our training set, uncertainties in observational measurements are intrinsic scatter between L_{IR} and other parameters.

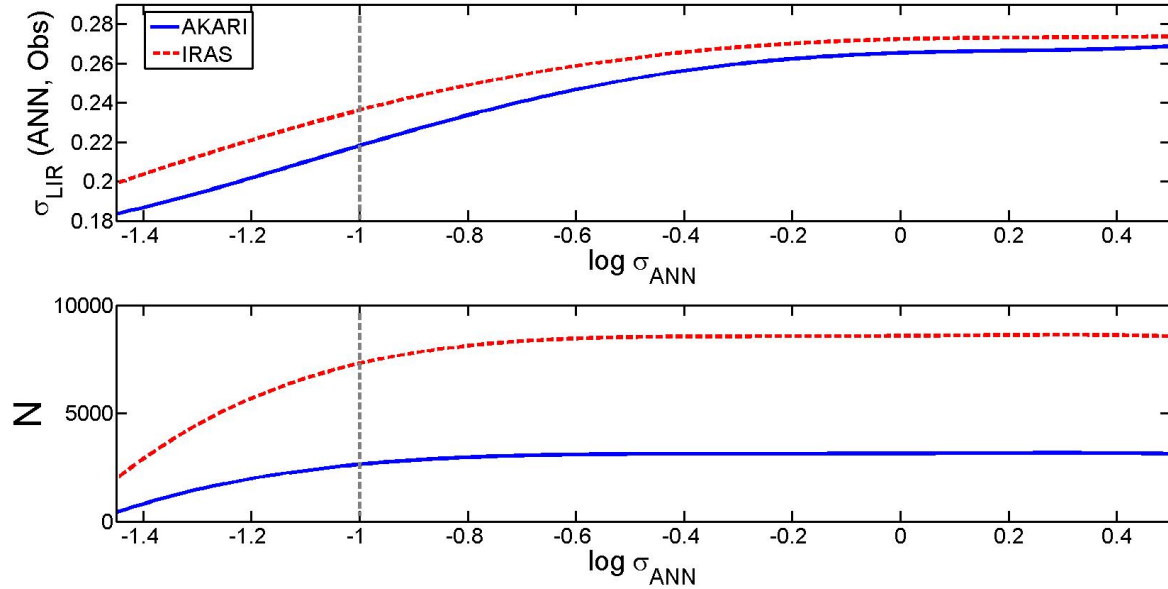


Figure 9. The effect on sample size (lower panel) and scatter (upper panel) as a function of σ_{ANN} threshold for the two independent validation sets (IRAS and AKARI). More stringent (smaller) thresholds in σ_{ANN} leads to a smaller scatter in the prediction of L_{IR} by the ANN, but reduces the size of the sample. A nominal requirement of $\sigma_{\text{ANN}} < 0.1$ (vertical dashed lines) is adopted for this work as a balance between sample size and scatter.

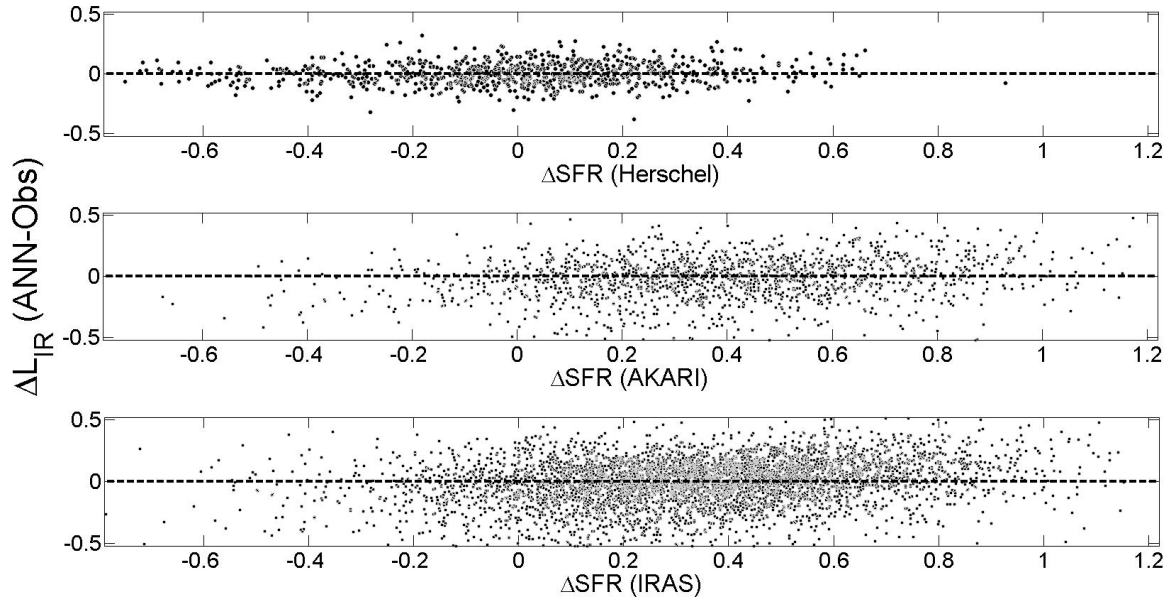


Figure 13. The accuracy of the ANN L_{IR} prediction as a function of ΔSFR , the offset of a galaxy from the star forming main sequence. In general, the ANN is able to robustly predict L_{IR} not only for galaxies on the main sequence ($\Delta \text{SFR} \sim 0$) but also for outliers. For (rare) galaxies with very enhanced SFRs ($\Delta \text{SFR} > 0.8$) there is tendency for the ANN to modestly over-predict the L_{IR} , due to the lack of galaxies in the training set in this regime.

5 COMPARISON WITH SDSS SFRS

In the previous sections, we have described the training and validation of artificial neural networks that may be used to predict the infra-red luminosities of galaxies. We have demonstrated that the trained networks perform well on independent datasets, that we are able to reject galaxies with poorly predicted L_{IR} via the imposition

of a σ_{ANN} threshold, and that the L_{IR} predictions are well suited for galaxies dominated by either star formation or AGN.

We are now ready to apply the trained and validated networks to the SDSS in order to predict their infra-red luminosities. Specifically, we apply the trained ANN to the $\sim 332,000$ galaxies for which all requisite training parameters are available. In Figure 14 we show the distribution of the L_{IR} values predicted for these 331,926 SDSS galaxies and the associated errors (described in Sec-

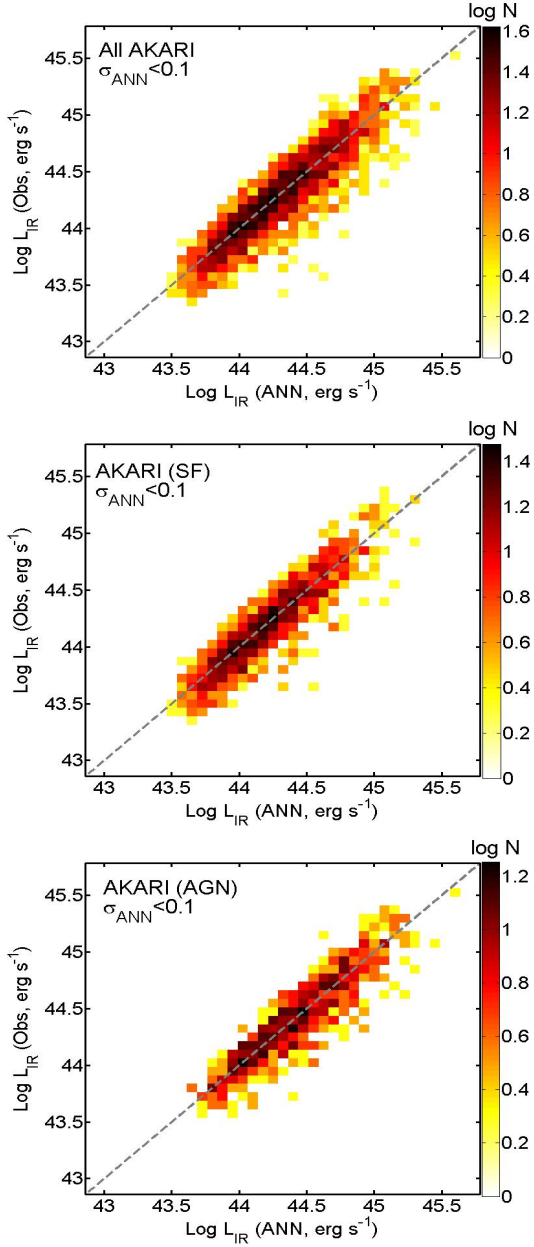


Figure 11. A comparison between the observed and predicted L_{IR} for the AKARI sample; all panels are colour coded by galaxy density and have an error cut of $\sigma_{ANN} < 0.1$. The top panel shows all galaxies, and the middle and lower panels distinguish the star forming and AGN galaxies respectively. The scatter for the star-forming and AGN galaxies is comparable: 0.23 and 0.25 dex, respectively.

tion 3.2). Of these galaxies, 128,507 are AGN. The infra-red luminosities and associated network error are presented in an online catalog that accompanies this paper. An excerpt from the catalog, representing its first 10 lines, is given in Table 2. For completeness, all target galaxies are listed, but 247,137 SDSS galaxies pass the $\sigma_{ANN} < 0.1$ dex criterion that we have adopted in this paper, of which 78,039 are classified as AGN (Kauffmann et al. 2003, $S/N \geq 1$).

In order to compare the predicted L_{IR} from the ANN to the SFRs derived from the SDSS spectra, we use Eqn. 1 to convert the predicted infra-red luminosities to star formation rates. In the

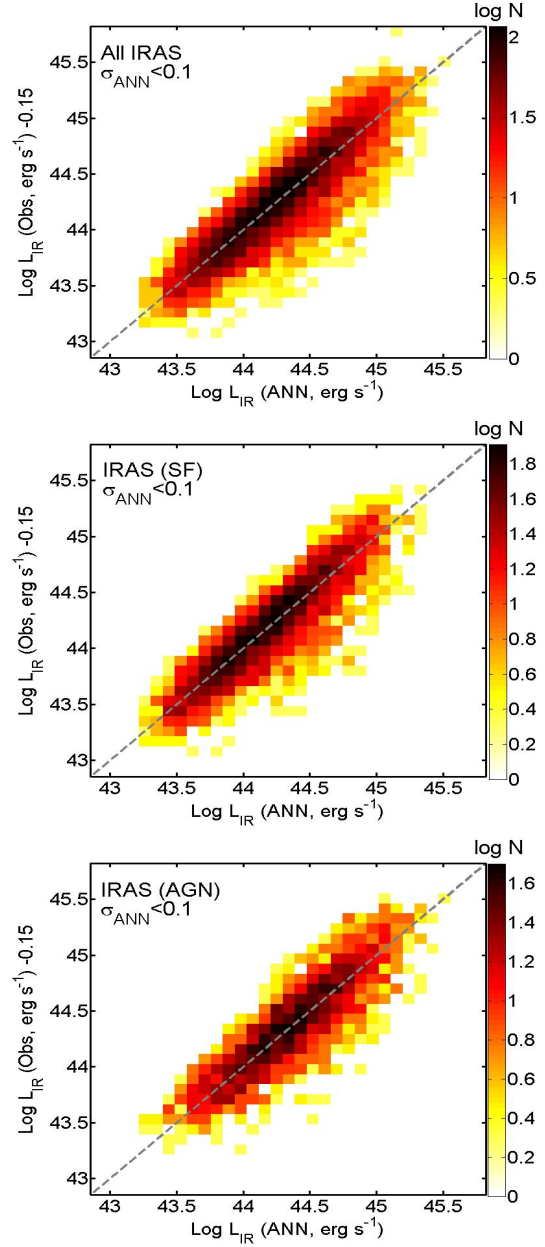


Figure 12. A comparison between the observed and predicted L_{IR} for the IRAS sample after both a 0.15 dex offset has been applied to bring the values into line with the other catalogs and calibrations used in this paper, and after a 0.1 dex cut in ANN error has been applied. The top, middle and lower panels show all, star forming and AGN galaxies respectively. The scatter for the star-forming and AGN galaxies is comparable: 0.20 and 0.24 dex, respectively.

top panel of Fig. 15 we show the scatter in the difference between the SFR derived from the ANN-predicted L_{IR} , and the SFR derived from aperture corrected SDSS spectra for star-forming galaxies only. As shown by Rosario et al. (2015), we expect these two SFR indicators to be in good agreement. In the lower panel of Fig. 15 we show how the sample size is affected by varying the σ_{ANN} threshold. Taken together, the two panels of Fig. 15 demonstrate that a cut at $\sigma_{ANN}=0.1$ is a good balance between sample size and accuracy. Stricter cuts yield a smaller scatter in the difference between SFR indicators, at the expense of sample size.

Table 2. Catalog of ANN predicted L_{IR} for SDSS galaxies. The first 10 entries are shown here; the full catalog is available in the online material that accompanies this paper.

SDSS objID	RA (deg.)	Dec. (deg.)	z	$\log L_{IR}$ (erg s^{-1})	σ_{ANN}
587722953304310243	237.26196	0.25983	0.03464	43.34	0.07
587722953304179097	236.88773	0.39001	0.11340	44.22	0.05
587722953304179083	236.88157	0.34449	0.03292	42.86	0.12
587722953304113519	236.77592	0.34773	0.03334	43.15	0.09
587722953303917041	236.36319	0.21511	0.10203	44.00	0.08
587722953303916807	236.22179	0.40430	0.03331	43.21	0.09
587722953304375633	237.28486	0.41628	0.19134	44.81	0.14
587722953304572300	237.81142	0.29300	0.03221	43.21	0.14
587722953304572365	237.86590	0.23560	0.08777	43.85	0.03
587722953304834385	238.37377	0.33674	0.09379	44.39	0.04

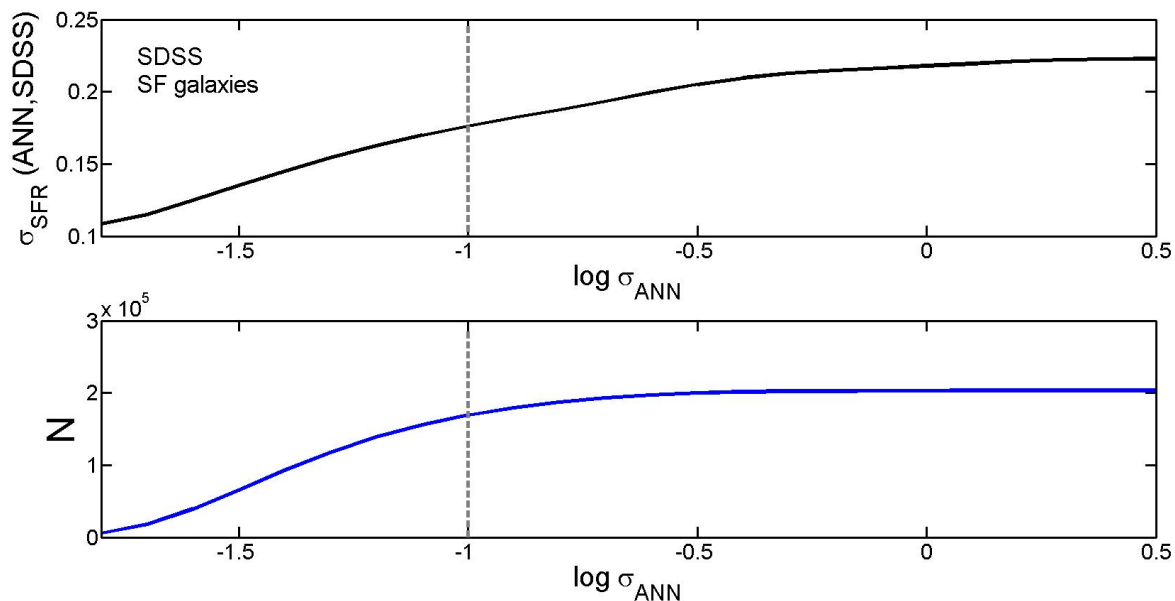


Figure 15. The effect on sample size (lower panel) and scatter (upper panel) as a function of σ_{ANN} threshold on the SDSS sample. The nominal requirement of $\sigma_{ANN} < 0.1$ adopted for this work is shown by a vertical dashed line in both panels.

To further understand the impact of the σ_{ANN} criterion, in the top panel of Figure 16 we compare the SFRs derived from our L_{IR} predictions to all $\sim 332,000$ SDSS galaxies with MPA/JHU star formation rates, with no error requirement imposed. The points are colour-coded by the ANN error (recall, this is a metric of the confidence of the ANN prediction based on the scatter from 20 trained networks). The top panel of the figure includes all galaxies, regardless of emission line classification. The majority of galaxies follow the 1:1 line (dashed line), and these are also seen to be the cases with the smallest associated ANN uncertainties. Galaxies with larger σ_{ANN} yield a larger scatter around the 1:1 line. There is also a clear population of galaxies with large σ_{ANN} that lie preferentially below the 1:1 line, i.e. where the SDSS SFR is lower than the L_{IR} derived value by an order of magnitude or more.

In the middle and lower panels of Figure 16 we now impose a 0.1 dex error cut, and distinguish the star-forming and AGN dominated galaxies (middle and lower panels respectively). The SFRs derived from the L_{IR} for star-forming galaxies are seen to be in excellent agreement with those derived from SDSS; the scatter is

0.17 dex for the 169,098 star forming galaxies that pass the error threshold (see also Fig. 15). However, even with the error cut, the lower panel of Figure 16 shows a persistent disagreement between the SDSS and ANN L_{IR} -based SFRs for the 78,039 AGN that pass the same $\sigma_{ANN} < 0.1$ dex threshold, in the sense that SDSS SFRs are lower than those derived from the L_{IR} by typically ~ 0.5 dex (a factor of three). The disagreement between the methods increases as the SFRs decline, although the discrepancy persists even at the highest SFRs of the sample.

The discrepancy shown in the lower panel of Figure 16 could be indicative of a problem with the ANN predictions of L_{IR} in AGN galaxies. However, the results presented in Section 4 demonstrate successful validation of the network with 3 different IR datasets (Herschel, AKARI and IRAS). The robustness of the network predictions in all our tests indicates that it may be the SDSS SFRs that are under-estimated in many of the AGN galaxies plotted in Figure 16 (which, it should be noted, is only a subset of all the AGN in the SDSS). Indeed, an apparent under-estimate of SDSS SFRs compared to L_{IR} SFRs has been recently reported by Rosario et al.

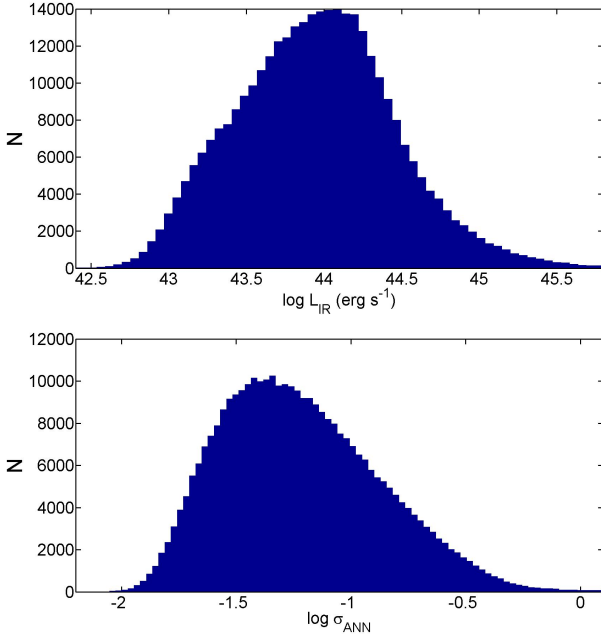


Figure 14. The distribution of the ANN-derived L_{IR} values for SDSS galaxies and the associated errors.

(2015) for the AGN, composite and low SFR galaxies in the original Herschel Stripe 82 data (see also Fan et al. 2013 for a similar result in the H-ATLAS SDP data). Rosario et al. (2015) show that there is an increasing disagreement between Herschel and SDSS SFRs as the error on the latter increases, indicating that the discrepancy is an Eddington bias caused by the limit in Herschel’s sensitivity. With a deeper IR dataset, we would expect to see a symmetric scatter in the comparison between SDSS galaxies with large errors and Herschel, but with the current IR detection limits, we only see one side of this distribution (galaxies on the other side of the distribution are not detected by Herschel). This scenario is confirmed by Rosario et al. (2015) with a Monte Carlo simulation of the SDSS error distribution and a comparison of the Herschel detection limit.

The results of Rosario et al. (2015) suggest that the offset between SDSS SFRs and those derived through ANN predictions of the L_{IR} for AGN galaxies (lower panel of Figure 16) is likely also to be due to the uncertainties in the former and the detection threshold of the latter. We test this hypothesis in Figure 17, where we show again the comparison between SFRs determined from our L_{IR} ANN predictions and those from the SDSS. These are the same galaxies shown in Fig. 16, but now colour coded by the error on the SDSS SFR. The star forming galaxies, which we have already shown in the middle panel of Fig. 16 exhibit a universally good agreement between the ANN and SDSS, all have relatively small SFR errors, typically <0.3 dex. However, there is a large spread in the SDSS SFR errors in the AGN population (Fig. 17, lower panel). Approximately 7 per cent of AGN have errors <0.3 dex, the median error is 0.5 dex and a significant number of galaxies with AGN have errors as large as 0.7–0.8 dex. A striking result of Fig. 17 is that as the error in the SDSS SFR increases, the disagreement with the ANN SFR also increases, and the offset is very similar to the error in the SDSS SFR. This demonstrates that the errors on the SDSS SFRs have been well determined. The distribution of points in the lower panel of Fig. 17 is therefore the result of the same Eddington bias seen in the Herschel training set, that leads to an apparent one-sided scatter in the comparison as the error in the SDSS SFR increases.

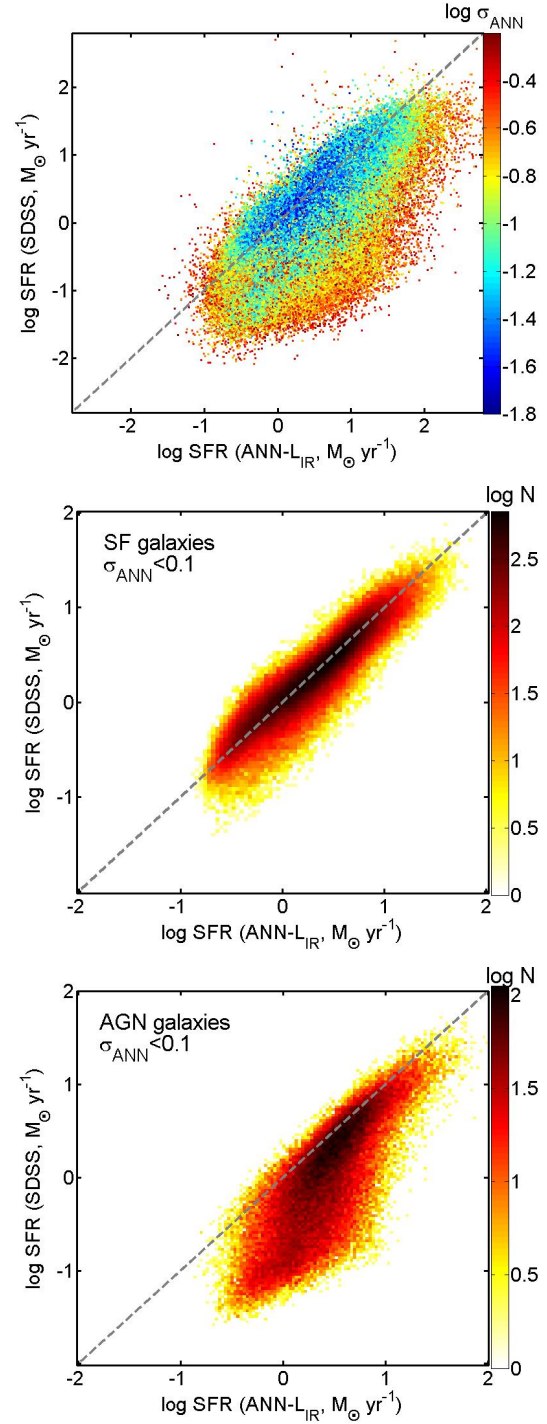


Figure 16. SDSS SFRs compared to the SFRs (Eqn 1) derived for our predicted infra-red luminosities. Top panel: SFRs for $\sim 332,000$ galaxies with L_{IR} predictions, with points colour coded by the ANN uncertainty (σ_{ANN}), derived from the scatter amongst 20 trained networks. In the middle and lower panels we show only galaxies with $\sigma_{ANN} < 0.1$. The colour coding represents the number of galaxies in each cell. The middle and lower panels show the SFRs for star-forming and AGN dominated galaxies, respectively.

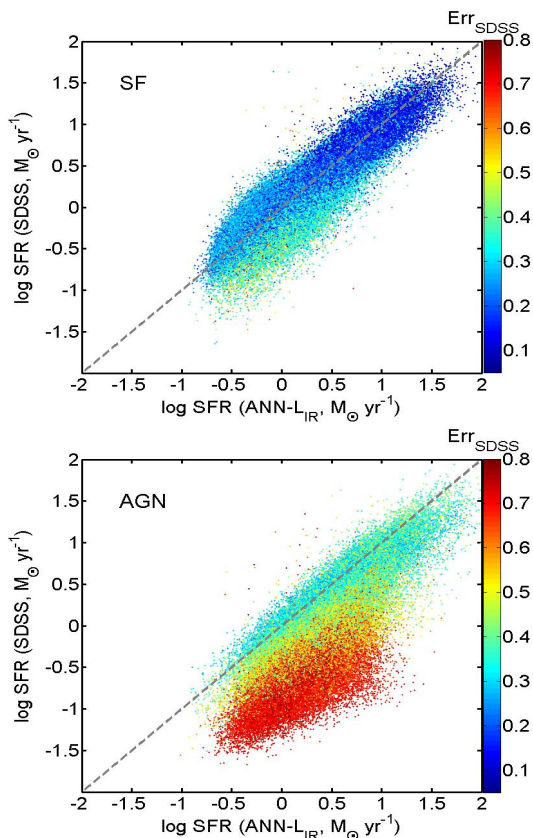


Figure 17. The same as Figure 16 for star forming and AGN galaxies (upper and lower panels respectively), but now colour coded by the error in the SDSS SFR.

Galaxies that scatter above the 1:1 line are not detected by the Herschel training set, and therefore do not have ANN predictions made. We therefore conclude that the SFRs from the ANN are robust (as supported by our validation tests), and that the discrepancy with the SDSS values is due to the typically large uncertainties in the latter. Our results and those of Rosario et al. (2015) highlight the niche of FIR-based SFRs, which can yield accurate values in regimes where the optical determinations have large associated errors.

6 SUMMARY

Based on a sample of 1136 galaxies identified in a cross-match between the SDSS and Herschel Stripe 82 Survey, we have trained an artificial neural network to predict IR luminosities based on 23 input parameters measured from SDSS imaging and spectroscopy. The scatter in the predicted L_{IR} for a self-validation test is <0.1 dex for both star-forming and AGN dominated galaxies. The network performance is validated on two independent datasets: the IRAS and AKARI all sky surveys, which have both been matched to SDSS galaxies. The scatter between the predicted and observed L_{IR} for both surveys is ~ 0.25 dex, after imposing an uncertainty threshold of $\sigma_{ANN} < 0.1$. We demonstrate that the ANN is able to predict L_{IR} for both star-forming and AGN dominated galaxies with similar scatter. The ANN is also able to accurately predict the L_{IR} (and hence SFR) even for galaxies lying significantly off the star-forming main sequence.

The trained networks are applied to $\sim 332,000$ SDSS galaxies for which all 23 input parameters are available, including $\sim 129,000$

AGN. Of these $\sim 332,000$ galaxies, 247,137 have $\sigma_{ANN} < 0.1$ dex, including $\sim 78,000$ AGN. We provide a catalog of the ANN predicted infra-red luminosities and their uncertainties (σ_{ANN}). The SFRs inferred from the ANN L_{IR} predictions are in excellent agreement with SDSS spectroscopic SFRs for star-forming galaxies. However, for the AGN with L_{IR} predictions, the SDSS SFR are apparently under-estimated by up to an order of magnitude, even when the uncertainty threshold has been imposed. It is demonstrated that this apparent under-estimate is due to larger uncertainties in the SDSS SFRs for AGN galaxies, which are based on D_{4000} , and the detection threshold in the training set. The L_{IR} predictions provided here can therefore be used to obtain more accurate SFR measurements in AGN, or in weak emission galaxies where there exist large uncertainties in the SDSS derived values (Fan et al. 2013; Rosario et al. 2015).

ACKNOWLEDGMENTS

We are grateful to Ho Seong Hwang for providing his catalogs of AKARI and IRAS fluxes for matched SDSS galaxies. SLE acknowledges the receipt of an NSERC Discovery Grant.

Funding for the SDSS and SDSS-II has been provided by the Alfred P. Sloan Foundation, the Participating Institutions, the National Science Foundation, the U.S. Department of Energy, the National Aeronautics and Space Administration, the Japanese Monbukagakusho, the Max Planck Society, and the Higher Education Funding Council for England. The SDSS Web Site is <http://www.sdss.org/>.

The SDSS is managed by the Astrophysical Research Consortium for the Participating Institutions. The Participating Institutions are the American Museum of Natural History, Astrophysical Institute Potsdam, University of Basel, University of Cambridge, Case Western Reserve University, University of Chicago, Drexel University, Fermilab, the Institute for Advanced Study, the Japan Participation Group, Johns Hopkins University, the Joint Institute for Nuclear Astrophysics, the Kavli Institute for Particle Astrophysics and Cosmology, the Korean Scientist Group, the Chinese Academy of Sciences (LAMOST), Los Alamos National Laboratory, the Max-Planck-Institute for Astronomy (MPIA), the Max-Planck-Institute for Astrophysics (MPA), New Mexico State University, Ohio State University, University of Pittsburgh, University of Portsmouth, Princeton University, the United States Naval Observatory, and the University of Washington.

REFERENCES

- Andreon, S., Gargiulo, G., Longo, G., Tagliaferri, R., Capuano, N., 2000, MNRAS, 319, 700
- Ball, N. M., Loveday, J., Fukugita, M., Nakamura, O., Okamura, S., Brinkmann, J., Brunner, R. J., 2004, MNRAS, 348, 1038
- Battiti, R., Neural Computation, 1992, 4, 141
- Bishop, C. M., 2007, Pattern Recognition and Machine Learning, 2007, Springer
- Bluck, A. F. L., Mendel, J. T., Ellison, S. L., Moreno, J., Simard, L., Patton, D. R., Starkeburg, E., 2014, MNRAS, 441, 599
- Brinchmann, J., Charlot, S., White, S. D. M., Tremonti, C., Kauffmann, G., Heckman, T., Brinkmann, J., 2004, MNRAS, 351, 1151
- Buat, V., et al., 2010, MNRAS, 409, 1
- Charlot, S., & Longhetti, M., 2001, MNRAS, 323, 887
- Chary, R., & Elbaz, D., 2001, ApJ, 556, 562
- Chen, S., Cowan, C. F. N., Grant, P. M., IEEE Transactions on Neural Networks, 1991, 2, 302

- Cheung, E., et al., 2012, *ApJ*, 760, 131
- Dale, D. A., & Helou, G., 2002, *ApJ*, 576, 159
- Dariush, A., et al., 2011, *MNRAS*, 418, 64
- De Jesus, O., & Hagan, M. T., 2007, *IEEE Transactions on Neural Networks*, 2007, 18, 14
- Dominguez Sanchez, H., et al., 2012, *MNRAS*, 426, 330
- Eales, S., et al., 2010, *PASP*, 122, 499
- Ellison, S. L., Nair, P., Patton, D. R., Scudder, J. M., Mendel, J. T., Simard, L., 2011, *MNRAS*, 416, 2182
- Fan, D.-X., Li, J.-R., Pan, Z.-Z., Shi, F., Fang, G.-W., Kong, X., 2013, *ChA&A*, 37, 126
- Ferland, G., Korista, K., Verner, D., Ferguson, J., Kingdon, J., Verner, E., 1998, *PASP*, 110, 761
- Forbes, J. C., Krumholz, M. R., Burkert, A., Dekel, A., 2014, *MNRAS*, 438, 1552
- Gonzalez-Martin, O., et al., 2014, *A&A*, 567, 92
- Goto, T., 2005, *MNRAS*, 360, 322
- Goto, T., et al., 2011, *MNRAS*, 410, 573
- Griffin, M. J., et al., 2010, *A&A*, 518, 3
- Gunawardhana, M. L. P., et al., 2011, *MNRAS*, 415, 1647
- Gurkan, G., et al., 2015, *MNRAS*, in press
- Hatziminaoglou, E., et al., 2010, *A&A*, 518, L33
- Hwang, H. S., Elbaz, D., Lee, J. C., Jeong, W.-S., Park, C., Lee, M. G., Lee, H. M., 2010, *A&A*, 522, 33
- Hwang, H. S., et al. 2011, *A&A*, 535, 60
- Jeong et al., W.-S., 2007, *PASJ*, 59, 429
- Kauffmann, G., et al., 2003, *MNRAS*, 346, 1055
- Kawada, M., et al., 2007, *PASJ*, 59, 389
- Kennicutt, R.C. 1998, *ARA&A*, 36, 189
- Kennicutt, R.C., Evans, N. J., 2012, *ARA&A*, 50, 531
- Kennicutt, R. C., Tamblyn, P., Congdon, C. E., 1994 *ApJ*, 435, 22
- Keres, D., Katz, N., Weinberg, D. H., Dave, R., 2005, *MNRAS*, 363, 2
- Kewley, L. J., Dopita, M. A., Sutherland, R. S., Heisler, C. A., Trevena, J., 2001, *ApJ*, 556, 121
- Kewley, L. J., Geller, M. J., & Jansen, R. A., 2004, *AJ*, 127, 2002
- L'Huillier, B., Combes, F., & Semelin, B., 2012, *A&A*, 544, 68
- Lutz, D., 2014, *ARA&A*, 52, 373
- Marquardt, D., *SIAM Journal on Applied Mathematics*, 1963, 11, 431
- Matsuoka, K., & Woo, J.-H., 2015, *ApJ*, in press.
- Mendel, J. T., Palmer, M. J. D., Simard, L., Ellison, S. L., Patton, D. R., 2014, *ApJS*, 210, 3
- Mendel, J. T., Simard, L., Ellison, S. L., Patton, D. R., 2013, *MNRAS*, 429, 2212
- Moshir, M., Kopman, G., Conrow, T. A. O. 1992, *IRAS Faint Source Survey*, Explanatory supplement version 2
- Mullaney, J. R., Alexander, D. M., Goulding, A. D., Hickox, R. C., 2011, *MNRAS*, 414, 1082
- Murakami, H., et al., 2007, *PASJ*, 59S, 369
- Neal, R. M., 1996, *Lecture Notes in Statistics*, 118
- Neugebauer, G., et al., 1984, *ApJ*, 278, L1
- Netzer, H., et al., 2007, *ApJ*, 666, 806
- Obric, M., et al., 2006, *MNRAS*, 370, 1677
- Oliver, S. J., et al., 2012, *MNRAS*, 424, 1614
- Pei, Y., 1992, *ApJ*, 395, 130
- Pilbratt, G. L., et al., 2010, *A&A*, 518, 1
- Rosario, D. J., Mendel, J. T., Ellison, S. L., Lutz, D., Trump, J. R., 2015, *MNRAS*, submitted
- Saintonge, A., et al., 2012, *ApJ*, 758, 73
- Salim, S., et al. 2007, *ApJS*, 173, 267
- Sancisi, R., Fraternali, F., Oosterloo, T., van der Hulst, T., 2008, *A&ARv*, 15, 189
- Schawinski, K., et al., 2014, *MNRAS*, 440, 889
- Scudder, J. M., Ellison, S. L., Mendel, J. T., 2012, *MNRAS*, 423, 2690
- Simard, L., Mendel, J. T., Patton, D. R., Ellison S. L., McConnachie, A. W., 2011, *ApJS*, 196, 11
- Takeuchi, T. T., et al., 2010, *A&A*, 514, 4
- Takeuchi, T. T., & Ishii, T. T., 2004, *ApJ*, 604, 40
- Tan, J. C., 2000, *ApJ*, 536, 173
- Teimoorinia, H., 2012, *AJ*, 144, 172
- Teimoorinia, H., Bluck, A. F. L., & Ellison, S. L., 2015, *MNRAS*, submitted
- Teimoorinia, H., & Ellison, S. L., 2014, *MNRAS*, 439, 3526
- Viero, M. P., et al., 2014, *ApJS*, 210, 22
- Wang, L., Rowan-Robinson, M., 2009, *MNRAS*, 398, 109
- Wang, J., et al., 2012, *MNRAS*, 423, 3486
- Wang, L., Rowan-Robinson, M., Norberg, P., Heinis, S., Han, J., 2014, *MNRAS*, 442, 2739
- Willett, K. W., et al., 2015, *MNRAS*, 449, 820
- Wright, E. L., et al., 2010, *AJ*, 140, 1868